

The geothermal output of the Katla caldera estimated using DEM differencing and 3D iceflow modelling

by

Alexander H. Jarosch¹, Eyjólfur Magnússon², Anna Wirbel³, Joaquín M. C. Belart² and Finnur Pálsson²

¹ThetaFrame Solutions, Kufstein, Austria

²Institute of Earth Sciences, University of Iceland, Askja, Reykjavík, Iceland

³Institute of Atmospheric and Cryospheric Sciences, University of Innsbruck, Innsbruck, Austria

RH-02-20



UNIVERSITY OF ICELAND
INSTITUTE OF EARTH SCIENCES



Jarosch, A. H.; Magnússon, E.; Wirbel, A.; Belart, J. M. C.; Pálsson, F. *The geothermal output of the Katla caldera estimated using DEM differencing and 3D-iceflow modeling* RH-02-20, 2020, doi:10.5281/zenodo.3784657

The geothermal output of the Katla caldera estimated using DEM differencing and 3D iceflow modelling

Alexander H. Jarosch¹, Eyjólfur Magnússon², Anna Wirbel³, Joaquín M. C. Belart², and Finnur Pálsson²

¹*ThetaFrame Solutions, Kufstein, Austria*

²*Institute of Earth Sciences, University of Iceland, Askja, Reykjavík, Iceland*

³*Institute of Atmospheric and Cryospheric Sciences, University of Innsbruck, Innsbruck, Austria*

May 4th, 2020

1 Introduction

To estimate heat output from several cauldrons on Mýrdalsjökull ice-cap between the years 2016 and 2019, elevation changes from digital elevation models (DEMs) of the glacier surface, deduced from Pléiades optical satellite images, are compared with simulated topographical changes of the glacier surface over the same time period.

The simulation solves for ice flow using a Full-Stokes finite element model. Based on the estimated ice flow velocities the free surface of the glacier is transported in the flow over time. An inequality constrained solution procedure is used to enforce the naturally occurring boundary condition that the surface elevation of a glacier can not fall below the elevation of its bedrock.

Utilizing the computed topographical changes in a comparison with DEM data allows for an estimate of ice volume change differences. These differences are attributed to basal melting beneath each respective cauldron because the simulations do not include basal processes. Based on these volume change differences estimates of the required amount of heat energy to melt the missing ice volumes can be calculated.

2 Model Description

Within the model domain, two elevation fields are tracked: the ice surface elevation (S) and the bedrock elevation (B). Glaciers exist wherever $S > B$ within the model domain, elsewhere the landscape is considered to be ice-free ($S = B$). The natural constraint that the ice surface elevation can not fall below the bedrock elevation:

$$S \geq B, \quad (1)$$

must be fulfilled at every point in time and space within the model.

Velocities for the slow, gravity-driven flow of ice are computed with the stationary incompressible Stokes equations (see Jarosch, 2008; Wirbel et al., 2018, for details). In order to describe the evolution of the “free” surface as a consequence of ice motion and specific mass balance rate, the following advection equation is used:

$$\frac{\partial S}{\partial t} = -u_h \cdot \nabla_h S + u_z + \dot{a}, \quad (2)$$

where $u_h = (u_x, u_y)$ are the horizontal ice surface velocity components, u_z is the vertical ice surface velocity component and \dot{a} the specific surface mass balance rate in m s^{-1} . Eq. 2, which is known as the “kinematic boundary condition” in fluid dynamics (e.g. White, 2010), is here used in a glaciological context by including the specific mass balance rate (e.g. Hutter, 1983). Even though the model is capable of utilizing a time dependent mass balance rate, for the study here $\dot{a} = 0$ is assumed and all effects of actual mass balance processes are dealt with through a surface elevation bias correction (cf. Sect. 5).

Due to the constraint Eq. 1 puts on Eq. 2, the free-surface evolution of glaciers becomes a variational inequality (Kinderlehrer and Stampacchia, 1980), which requires adequate treatment to ensure mass conservation.

Details on the model implementation and model performance evaluation can be found in Wirbel and Jarosch (2020).

3 Model Tuning

Two parameters are to be estimated in the non-linear Stokes equation (e.g. Jarosch, 2008, eqs. 8 and 9) that forms the dynamic basis of the simulated ice motion. These two parameters are well known as the Glen rate factor A and the nonlinearity exponent n (e.g. Glen, 1955). Assuming $n = 3$ (e.g. Cuffey and Paterson, 2010) leaves A to be estimated.

Surface velocity measurements at a stake ("K01d" measured in 2018) and from two continuous GPS stations ("K2" in 2018 and "K6" in 2017), which are all slow moving, are used to tune for A (see Fig. 2 for locations.) The mean motion vectors from the GPS stations were calculated outside jökulhlaup periods to ensure no influence from basal processes on the tuning process. It is assumed that the 2017 data at "K6" is valid for 2018 as the cauldron shape of "C6" did not change significantly between 2017 and 2018.

Based on simulated surface velocities utilizing the 2018 surface DEM and the 2019 bedrock DEM (cf. Tab. 1), four different performance measure can be calculated, which are displayed in Fig. 1.

The root mean squared error, mean bias and skill score all indicate that $A = 2.6 \times 10^{-24} \text{ Pa}^{-3} \text{ s}^{-1}$ is the most favourable value. Pearson's correlation coefficient values are all above 0.99 and do not indicate a clear favourite. In the following simulations $n = 3$ and $A = 2.6 \times 10^{-24} \text{ Pa}^{-3} \text{ s}^{-1}$ are used as the Glen's flow law parameters.

4 Input Data Processing

Several DEM datasets are required for the simulations to be carried out which are listed in Tab. 1.

Preexisting data holes in the surface datasets were patched with 2010 Lidar data as well as 2014 surface data. When calculating ice thickness data, $H = S - B$, quite often negative values are found outside the central region of Mýrdalsjökull. Such negative ice thickness values indicate that B (the bedrock) is located higher than S (the surface). The 2019 bedrock data (cf. Tab. 1) was corrected individually for each surface dataset to ensure that $H \geq 20 \text{ m}$ for the whole model domain (cf. Fig. 2). For these ice thickness corrections the respective surface dataset was kept fixed and the accompanying bedrock data was adjusted.

An unstructured computational mesh with variable mesh size is used for the simulations. 50 m mesh size is used within the focus regions (cf. Fig. 2) which gradually decreases towards 200 m on the edges of the model domain. These mesh size variations ensure high resolution in the areas of interest, where input data quality is high as well. At the same time, a variable mesh size optimizes computational cost spent on the simulations.

5 Results

Simulations are carried out for different time intervals based on the input datasets from Tab. 1 and the tuned model parameters (cf. Sect. 3). An overview of the performed model runs is given in Tab. 2. Between the years 2018 and 2019 a longer time period is used at cauldrons C10 and C11 to estimate heat output. The respective simulation "S2018b" (cf. Tabs 2 and 3) is 25 days longer and uses "Surface 2019 B" (cf. Tab. 1) to calculate surface elevation differences. This longer time period has been chosen due to a jökulhlaup occurring between September 28th and October 3rd (Magnússon et al., 2020) from those two cauldrons.

Starting from an input data pair (i.e. surface and bedrock DEM), the model described in Sect. 2 is used to predict glacier surface evolution over time. When the target date (i.e. the next years surface DEM date) is reached, a difference map between modelled prediction and actual surface data is calculated (see Fig. 3 as an example). These difference maps are created on regular, 20 m spatial resolution grids, on which the model data has been interpolated.

In this step an elevation bias correction is applied to minimize the elevation difference between the model-data difference map and the respective DEM data in a certain area around each cauldron. The bias correction is meant to compensate for elevation changes caused by surface mass balance, errors in both initial and final DEM as well as model simulation errors. In Fig. 2 the mass balance bias correction areas are plotted in orange. These areas correspond to the nearest ice divides (C16 and NB as well C10 and C11) and/or the nearest area outside the corresponding cauldron area where the difference between observed and simulated elevation change is approximately a spatial constant. The applied bias correction values are listed in Tab. 4.

Based on the computed surface elevation difference maps, individual focus regions are then integrated to get ice volume differences. Assuming a latent heat of fusion $L = 333550.0 \text{ J kg}^{-1}$ and density $\rho = 910 \text{ kg m}^{-3}$ for ice, the computed ice volume differences can be converted in thermal energy required to melt the respective ice volume. A time averaged heat flux is subsequently calculated by distributing the computed thermal energy equally over the

time period of the model simulation. Results for all model runs and focus regions are presented in Tab. 3. The total heat output for all modelled cauldrons varies between 462.4 ± 62.9 MW and 663.9 ± 73.1 MW over the three years period, with a mean annual heat flux of 582.6 ± 39.3 MW. Figures 3, 4, 5 and 6 display difference maps (model - DEM) for the respective years, corresponding to the four model runs (cf. Tab. 2). The annual mean bias (cf. Tab. 4) has been added to these maps to make them comparable.

Heat flux uncertainties are estimated based on uncertainty in the bias correction applied, obtained in the corresponding reference area. Uncertainty in ice volume lost beneath the cauldrons depends on how applicable the bias correction is, obtained from the reference area, for the corresponding cauldron area. In areas of well established bed DEM the spatial variability of the difference between the final simulated and observed glacier surface is generally low outside the cauldrons. We therefore assume ± 1 m uncertainty in the applied bias corrections for all cauldron areas. Based on focus region area (cf. Tab. 5) and assuming symmetric uncertainty, the uncertainty of ice mass lost beneath the cauldrons can be calculated for each focus region which are listed in Tab. 5. These ice mass uncertainties are converted to time averaged heat flux estimate uncertainties with the same method as described above and are given in Tab. 3. To propagate uncertainties¹ it is further assumed that heat flux uncertainties are normal distributed and the \pm uncertainty values listed are one sigma estimates from the error normal distribution.

Acknowledgements

This study was financed by the Icelandic research council (Rannís) through the project Katla Kalda (nr. 163391-051). Sveinbjörn Steinþórsson, Bergur Einarsson and Ásgeir Arnór Stefánsson as well as JÖRFÍ volunteers is thanked for their work during field trips on Mýrdalsjökull.

Pléiades imagery used to produce DEMs in 2016–2018 were acquired at research price thanks to the CNES ISIS program. The Pléiades imagery used to produce DEMs in 2019 were provided by CNES through CEOS (Committee on Earth Observation Satellites) support to the Iceland Volcanoes Supersite.

¹Uncertainty propagation is carried out automatically during the data analysis in Python (<https://uncertainties-python-package.readthedocs.io/>)

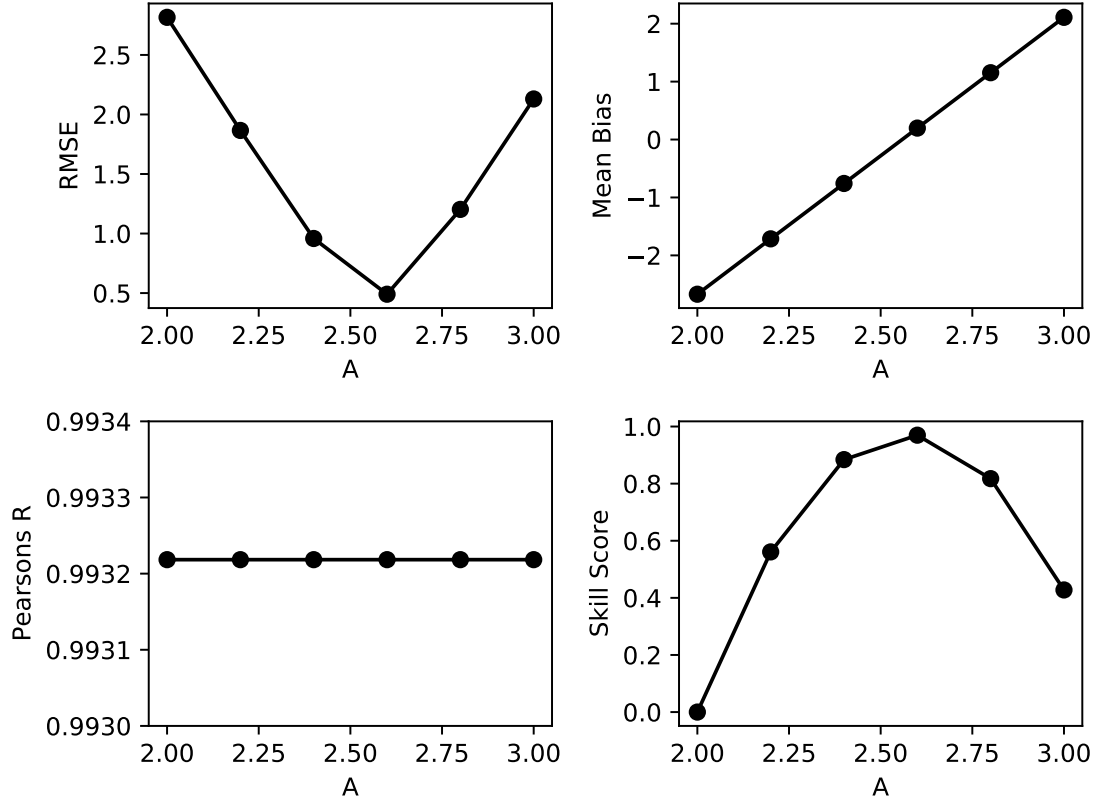


Figure 1: Tuning results for different rate factors A (in units of $10^{-24} \text{ Pa}^{-3} \text{ s}^{-1}$) based on surface velocities at "K01d", "K2" and "K6" from 2018. Clockwise from top-left, root mean squared error, mean bias, Pearson's R (Pearson's correlation coefficient) and skill score.

Name	Date	Filename according to Eyjólfur Magnússon
Surface 2016	2016.09.27	Myrdalsjokull_20160927_no_gcps-4x4m_fill20m_Int-ICP-DEM_bl_0_geoid_median_11x11_bl_med_2m_utgildi_vert_cor_mv_DEM_1sep2017_lagad_innan_oskju.grd
Surface 2017	2017.09.01	myrdalsjokull_20170901_no_gcps-4x4m_fill20m_int-dem_bl_ogildi_hor_shift_mv_lidar_4m_west_vert_cor_bl_3m_med_utgildi_geoid_fyllt_i_eydur_med_filt.grd
Surface 2018	2018.09.30	Myrdalsjokull_20180930_no_gcps-4x4m_fill20m_Int_JP2-DEM_geoid_shift_4m_south_plus_4p48m_bl_med_1m_utgildi_og_count_fyllt_med_14sept_cor_to_30sept_svlagad2.grd
Surface 2019 A	2019.09.28	Myrdalsjokull_20190928-4x4m_fill20m_Int-DEM_geoid_shift_4msouth_4mwest_hallandi_cor.grd
Surface 2019 B	2019.10.23	Myrdalsjokull_20191023-4x4m_fill20m_Int-DEM_geoid_hallandi_cor_4meast_4msouth.grd
Bedrock 2019	2019.10.XX	bed_oct2019.grd

Table 1: DEM datasets used in this study.

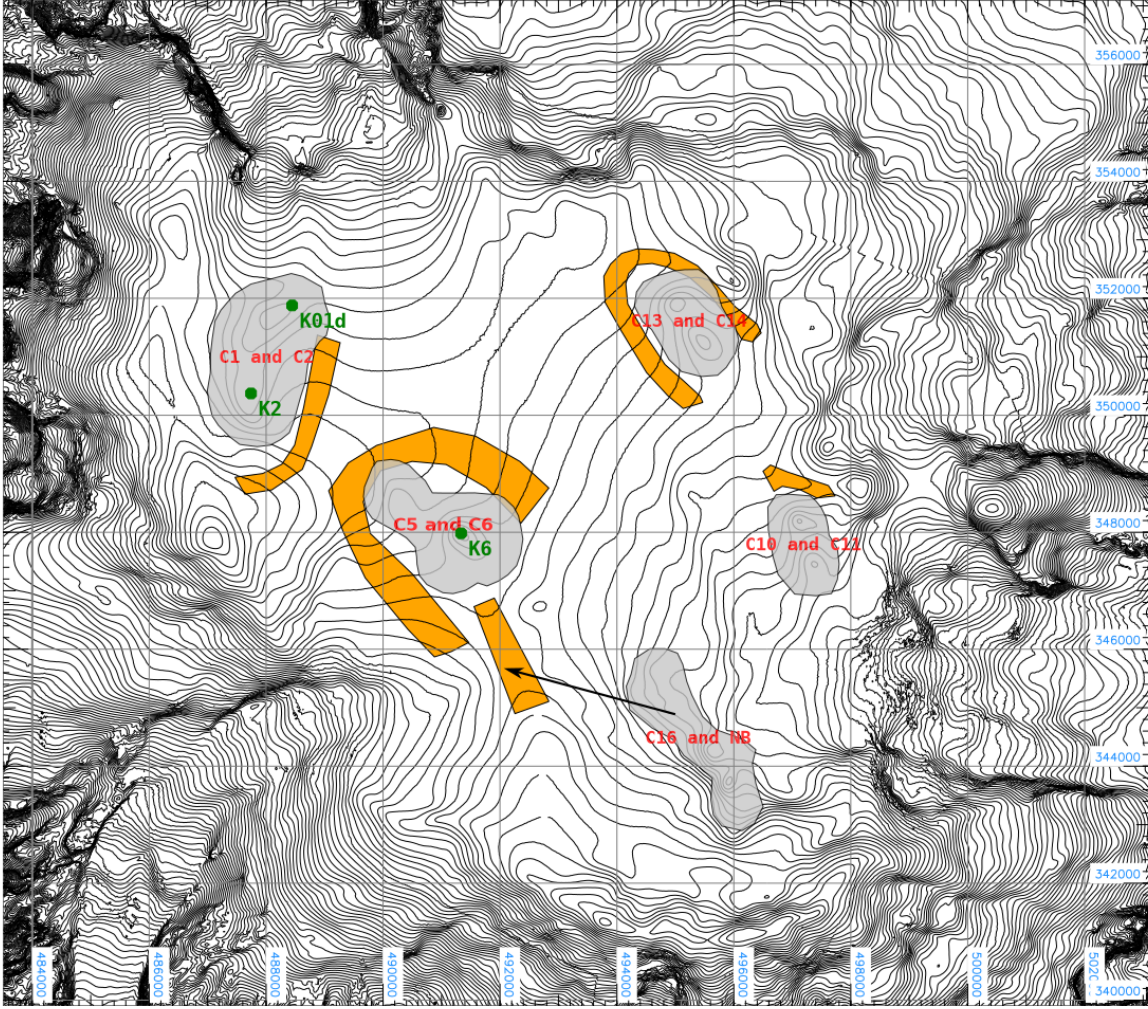


Figure 2: Overview map of the focus regions on Mýrdalsjökull ice-cap with contour lines of the 2018 September map. Glen's rate factor tuning locations are marked in green and the individual mass balance bias correction areas are in orange. For cauldrons "16 and neighbours" the mass balance bias correction area is indicated with an arrow.

Simulation Name	Start Date	End Date	Model Time Step [hours]	# Velocity Datasets	# Surface Datasets
S2016	2016.09.27	2017.09.01	678	12	99
S2017	2017.09.01	2018.09.30	788	12	116
S2018a	2018.09.30	2019.09.28	720	13	111
S2018b	2018.09.30	2019.10.23	720	13	117

Table 2: Simulations performed in this study. The model time step defines the creation of the velocity field data, surface elevation data is created on a substantially smaller time step which is dynamically adjusted by the model.

Name	Days [m]	C1 and C2 [MW]	C5 and C6 [MW]	C10 and C11 [MW]	C13 and C14 [MW]	C16 and NB. [MW]	Annual Total [MW]
S2016	339	198.2±46.2	70.3±38.5	102.6±17.1	88.6±23.0	204.3±30.1	663.9±73.1
S2017	394	160.2±39.7	51.3±33.1	31.5±14.7	89.7±19.8	129.7±25.9	462.4±62.9
S2018a	364	215.9±43.0	70.0±35.8	–	80.2±21.5	157.0±28.1	–
S2018b	389	–	–	98.5±14.9	–	–	–
S2018 total							621.5±67.9
Total mean							582.6±39.3

Table 3: This table displays the overall heat output from different cauldron regions over time. Time-span of model runs in days is displayed in the second column. The row labelled "S2018 total" displays the total sum for 2018, which is calculated by combining "S2018a" and "S2018b".

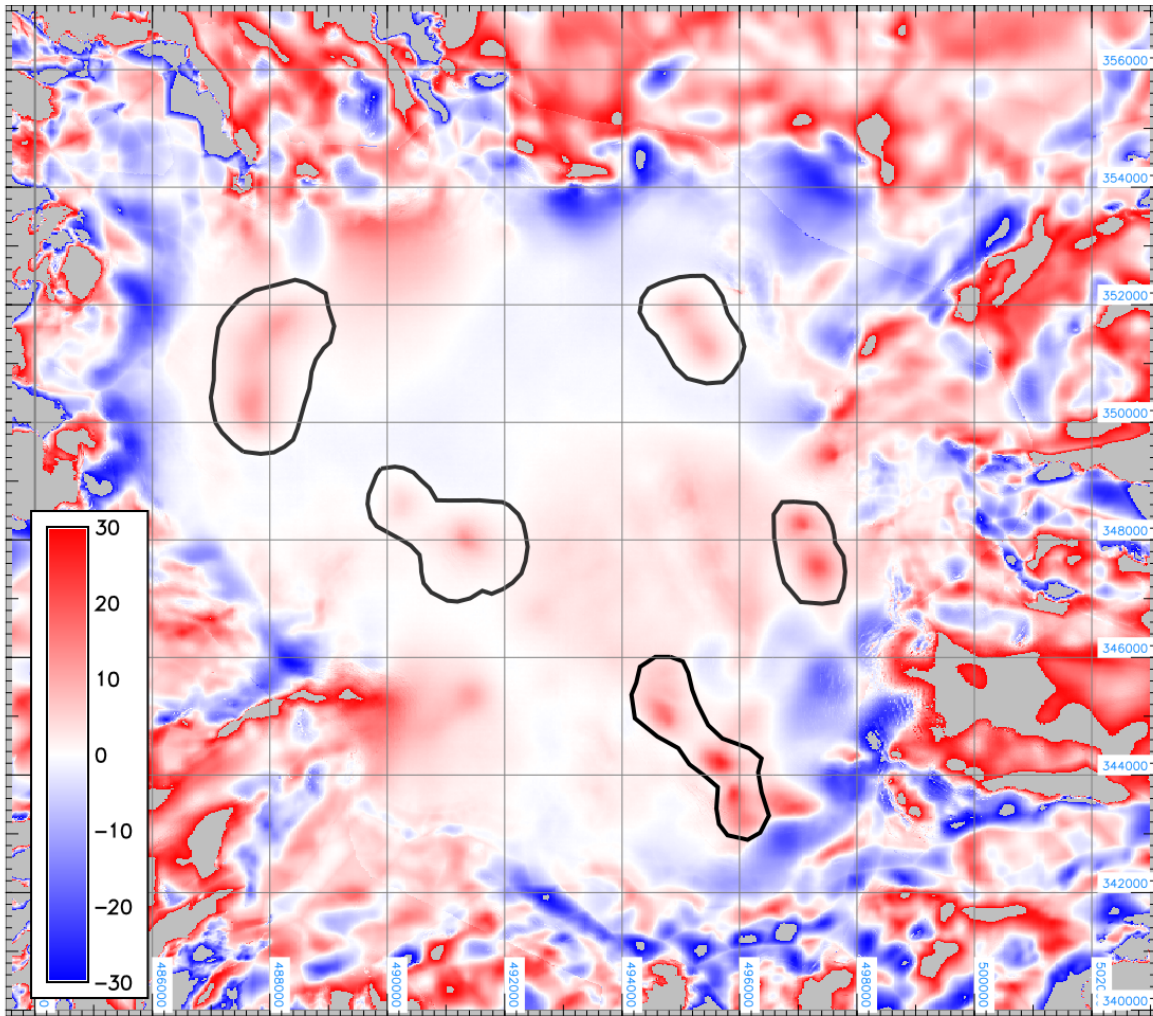


Figure 3: Difference map between model prediction and DEM data on 2017.09.01 in colors. Gray areas are outside the displayed data range. The mean bias according to Tab. 4 has been applied.

Property	C1 and C2	C5 and C6	C10 and C11	C13 and C14	C16 and NB.	Annual Mean
Bias corr. 2017 [m]	6.6099	6.1542	5.3134	7.3937	6.0517	6.3046
Bias corr. 2018 [m]	3.8119	3.9573	3.2617	5.7251	4.1501	4.1812
Bias corr. 2019 [m]	2.2583	2.5433	1.9695	3.6278	2.019	2.4836

Table 4: Bias corrections for the years 2017, 2018 and 2019 correspond to the end dates of the individual simulations. They are applied as "model elevation" - "DEM elevation" + "Bias corr." to compute the final, corrected difference maps.

Property	C1 and C2	C5 and C6	C10 and C11	C13 and C14	C16 and NB.
Focus Region Area [km ²]	4.4528	3.7107	1.6495	2.2221	2.9068
Ice mass uncertainty [1e9 kg]	±4.0521	±3.3767	±1.5010	±2.0221	±2.6452

Table 5: Area of individual focus regions which are used in the uncertainty estimates alongside ice mass uncertainty based on the symmetric ± 1 m elevation bias.

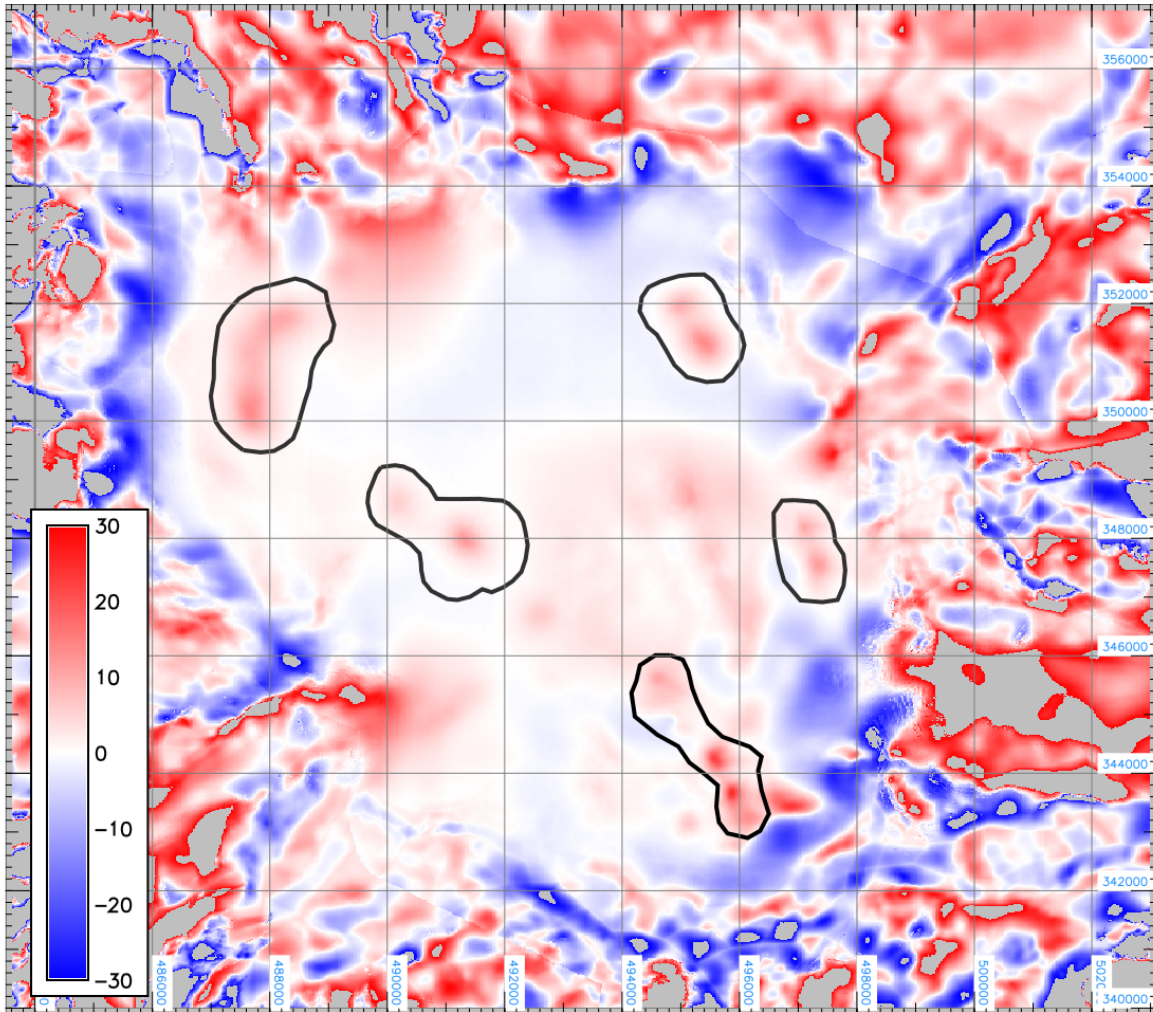


Figure 4: Difference map between model prediction and DEM data on 2018.09.30 in colors. Gray areas are outside the displayed data range. The mean bias according to Tab. 4 has been applied.

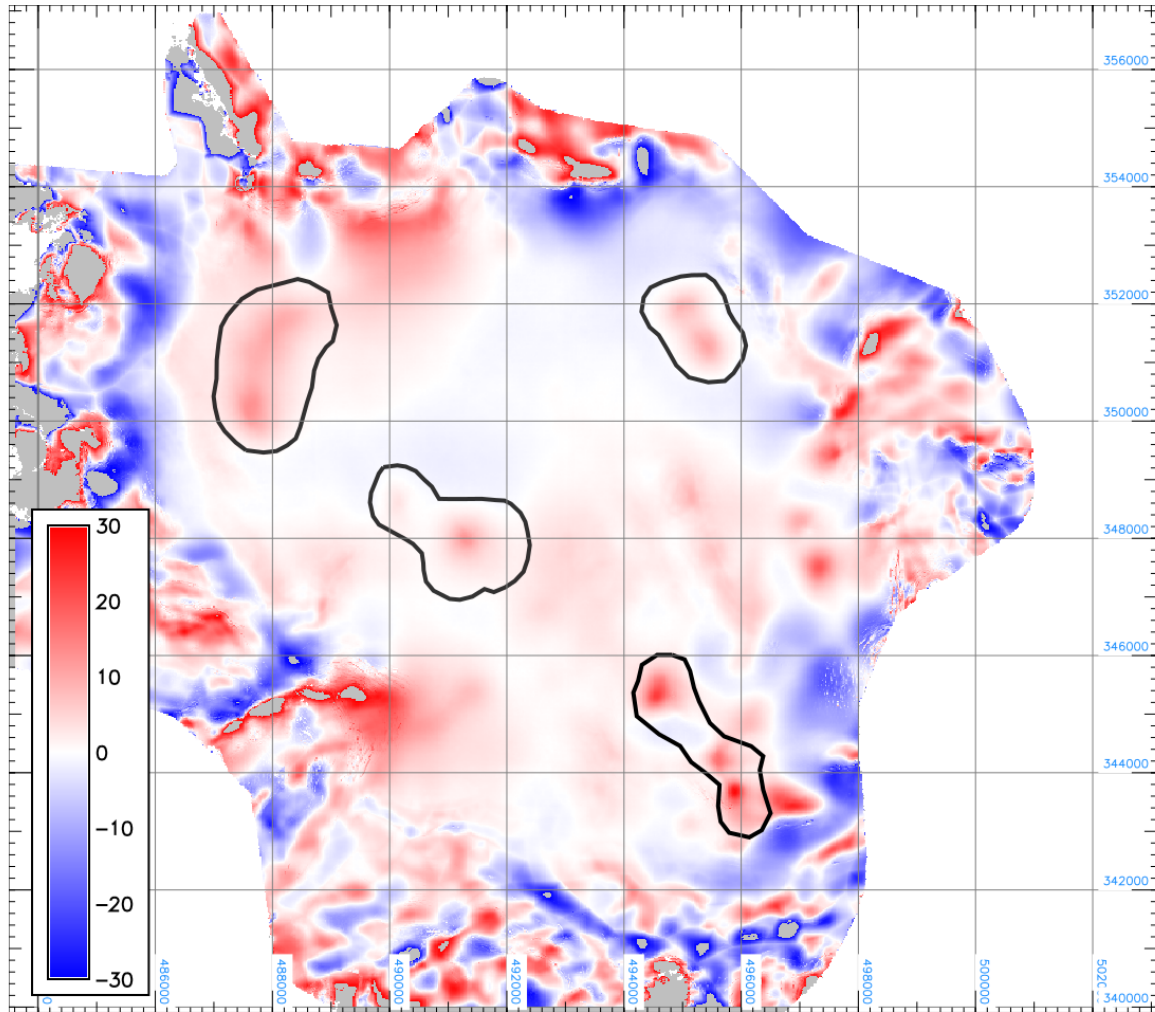


Figure 5: Difference map between model prediction and DEM data on 2019.09.28 in colors. Gray areas are outside the displayed data range. The mean bias according to Tab. 4 has been applied. This map is valid for cauldrons C1, C2, C5, C6, C13, C14, C16 and C16 neighbours.

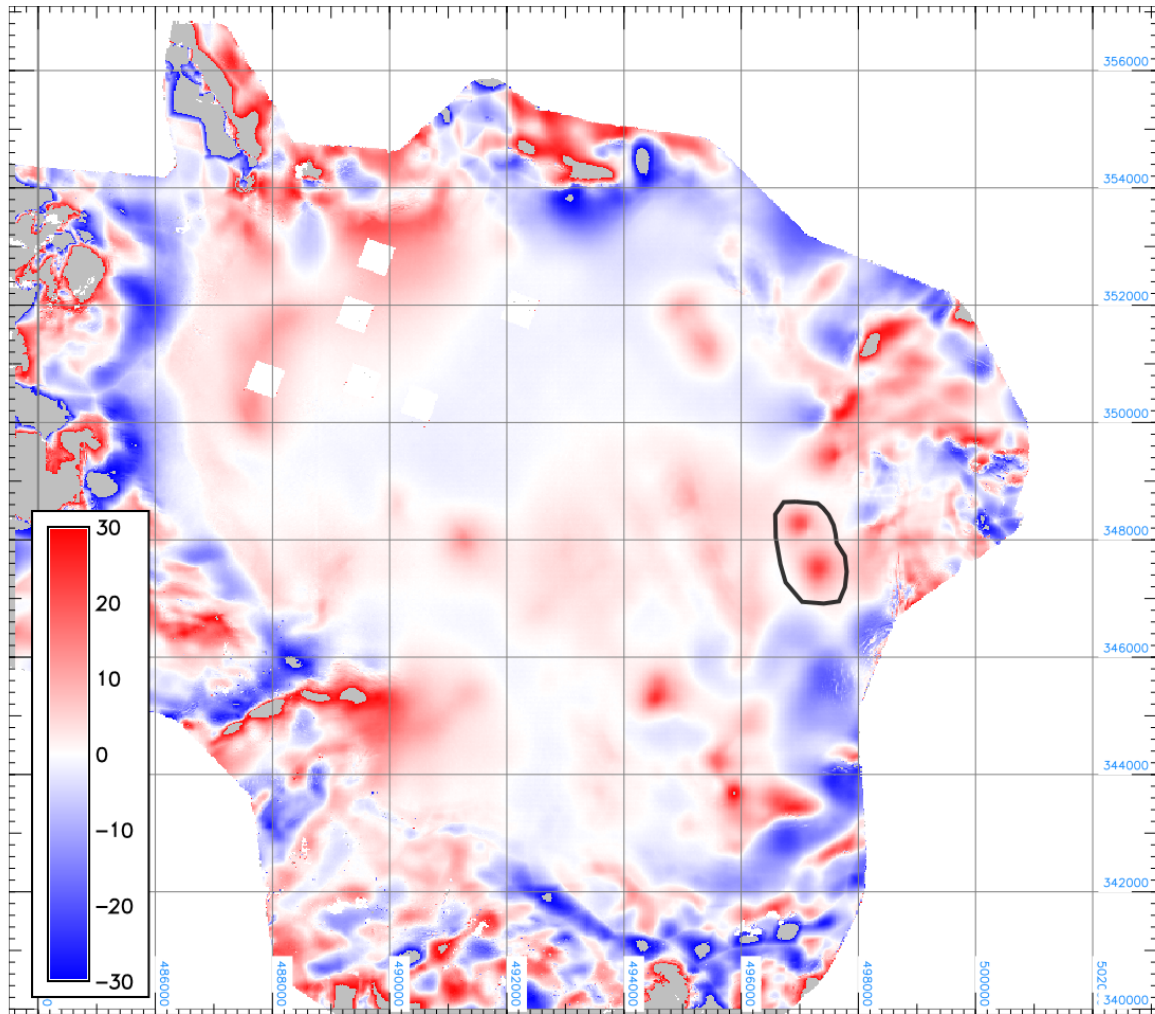


Figure 6: Difference map between model prediction and DEM data on 2019.10.23 in colors. Gray areas are outside the displayed data range. The mean bias according to Tab. 4 has been applied. This map is valid for cauldrons C10 and C11.

References

- Cuffey, K. M. and Paterson, W. S. B.: The Physics of Glaciers, Academic Press, Burlington, MA, 4th edn., 2010.
- Glen, J. W.: The creep of polycrystalline ice, Proceedings of the Royal Society of London A: Mathematical, Physical and Engineering Sciences, 228, 519–538, <https://doi.org/10.1098/rspa.1955.0066>, 1955.
- Hutter, K.: Theoretical glaciology: material science of ice and the mechanics of glaciers and ice sheets, D. Reidel Publishing Company, Dordrecht, Holland, 1983.
- Jarosch, A. H.: Ictools: A full Stokes finite element model for glaciers, Computers & Geosciences, 34, 1005–1014, <https://doi.org/10.1016/j.cageo.2007.06.012>, 2008.
- Kinderlehrer, D. and Stampacchia, G.: An introduction to variational inequalities and their applications, vol. 31, Siam, 1980.
- Magnússon, E., Pálsson, F., Belart, J. M. C., Einarsson, B., and Ófeigsson, B. G.: Próun vatnsgeyma undir sigkötllum Mýrdalsjökuls séð með íssjá, Tech. rep., Institute of Earth Sciences, University of Iceland and the Icelandic Met Office, 2020.
- White, F.: Fluid Mechanics, McGraw-Hill Science/Engineering/Math, seven edn., 2010.
- Wirbel, A. and Jarosch, A. H.: Free–Surface Flow as a Variational Inequality (evolve_glacier v1.1): Numerical Aspects of a Glaciological Application, Geoscientific Model Development Discussions, pp. XX, in review, gmd–2020–58, <https://doi.org/10.5194/gmd-2020-58>, 2020.
- Wirbel, A., Jarosch, A. H., and Nicholson, L.: Modelling debris transport within glaciers by advection in a full-Stokes ice flow model, The Cryosphere, 12, 189, <https://doi.org/10.5194/tc-12-189-2018>, 2018.